Fractal structures for the Jacobi Hamiltonian of restricted three-body problem

Guillaume Rollin, José Lages, Dima Shepelyansky

▶ **To cite this version:**

Guillaume Rollin, José Lages, Dima Shepelyansky. Fractal structures for the Jacobi Hamiltonian of restricted three-body problem. New Astronomy, 2016, 47, pp.97-104. 10.1016/j.newast.2016.02.010 . hal-01206372v2

HAL Id: hal-01206372
https://hal.science/hal-01206372v2

Submitted on 27 Mar 2016

HAL is a multi-disciplinary open access archive for the deposit and dissemination of scientific research documents, whether they are published or not. The documents may come from teaching and research institutions in France or abroad, or from public or private research centers.

L'archive ouverte pluridisciplinaire **HAL**, est destinée au dépôt et à la diffusion de documents scientifiques de niveau recherche, publiés ou non, émanant des établissements d'enseignement et de recherche français ou étrangers, des laboratoires publics ou privés.

Distributed under a Creative Commons Attribution - NonCommercial - NoDerivatives| 4.0 International License

Fractal structures for the Jacobi Hamiltonian of restricted three-body problem

G. Rollin[a], J. Lages[a], D. L. Shepelyansky[b]

[a] *Institut UTINAM, Observatoire des Sciences de l'Univers THETA, CNRS, Université de Franche-Comté, 25030 Besanon, France*
[b] *Laboratoire de Physique Théorique du CNRS, IRSAMC, Université de Toulouse, UPS, 31062 Toulouse, France*

Abstract

We study the dynamical chaos and integrable motion in the planar circular restricted three-body problem and determine the fractal dimension of the spiral strange repeller set of non-escaping orbits at different values of mass ratio of binary bodies and of Jacobi integral of motion. We find that the spiral fractal structure of the Poincaré section leads to a spiral density distribution of particles remaining in the system. We also show that the initial exponential drop of survival probability with time is followed by the algebraic decay related to the universal algebraic statistics of Poincaré recurrences in generic symplectic maps.

Keywords: Chaos, Celestial mechanics, Binaries, Galaxies: spiral

1. Introduction

The restricted three-body problem was at the center of studies of dynamics in astronomy starting from the works of Euler (1772), Jacobi (1836) and Poincaré (1890). The progress in the understanding of this complex problem in XXth and XXIth centuries is described in the fundamental books (Szebehely, 1967; Hénon, 1997, 2001; Valtonen and Karttunen, 2006). As it was proven by Poincaré (1890) in the general case this system is not integrable and only the Jacobi integral is preserved by the dynamics (Jacobi, 1836). Thus a general type of orbits has a chaotic dynamics with a divided phase space where islands of stability are embedded in a chaotic sea (Chirikov, 1979; Lichtenberg and Lieberman, 1992; Ott, 1993).

In this work we consider the Planar Circular Restricted Three-Body Problem (PCRTBP). This is an example of a conservative Hamiltonian system (in a synodic or rotating reference frame of two binaries) with two degrees of freedom. However, this is an open system since some trajectories can escape to infinity (be ionized) so that the general theories of leaking systems (Altmann et al., 2013) and naturally open systems (e.g. Contopoulos and Efstathiou, 2004) find here their direct applications. It is known that such open systems are characterized by strange repellers related to non-escaping orbits and by an exponential time decay of probability to stay inside the system. However, as we show, in the PCRTBP system with a divided phase space one generally finds an algebraic decay of probability of stay related to an algebraic statistics of Poincaré recurrences in Hamiltonian systems (see e.g. Chirikov and Shepelyansky, 1981; Karney, 1983; Chirikov and Shepelyansky, 1984; Meiss and Ott, 1985; Chirikov and Shepelyansky, 1999; Cristadoro and Ketzmerick, 2008; Shevchenko, 2010; Frahm, K. M. and Shepelyansky, D. L., 2010, and Refs. therein). This effect appears due to long sticking of trajectories in a vicinity of stability islands and critical Kolmogorov-Arnold-Moser (KAM) curves. Thus an interplay of fractal structures and algebraic decay in the PCRTBP deserves detailed studies.

Among the recent studies of the PCRTBP we point out the advanced results of Nagler (2004, 2005) where the crash probability dependence on the size of large bodies has been studied and the fractal structure of non-escaping orbits has been seen even if the fractal dimensions were not determined. This research line was extended in Astakhov and Farrelly (2004); Astakhov et al. (2005) with a discussion of possible applications to the Kuiper-belt and analysis of various types of orbits in Barrio et al. (2009); Zotos (2015). The analysis of orbits in three dimensional case is reported in Makó et al. (2010) and basin of escaping orbits around the Moon has been determined in de Assis and Terra (2014).

In this work we determine the fractal dimension of non-escaping orbits for the PCRTBP with comparable masses of heavy bodies and consider the properties of Poincaré recurrences and the decay probability of stay in this system. The system description is given in Section 2, the structure of strange repeller is analyzed in Section 3, the decay of Poincaré recurrences and probability of stay are studied in Section 4, a symplectic map description of the dynamics is given in Section 5, discussion of the results is presented in Section 6.

2. System description

The PCRTBP system is composed of a test particle evolving in the plane of a circular binary whose primaries have masses $m_1 = 1 - \mu$ and $m_2 = \mu$ with $m_1 > m_2$. In the synodic frame the dynamics of the test particle is given by the Hamiltonian

$$H(p_x, p_y, x, y) = \frac{1}{2}\left(p_x^2 + p_y^2\right) + yp_x - xp_y + V(x, y) \qquad (1)$$

Email addresses: rollin@obs-besancon.fr (G. Rollin), jose.lages@utinam.cnrs.fr (J. Lages), dima@irsamc.ups-tlse.fr (D. L. Shepelyansky)

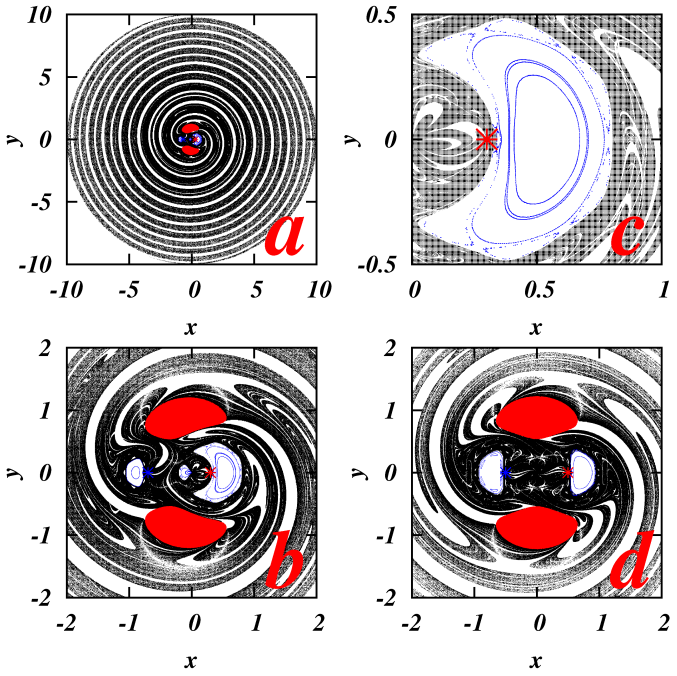

Figure 1: (x, y) - Poincaré sections of the Jacobi Hamiltonian (1) with $\dot{r} = 0$ and $\dot{\phi} < 0$. Poincaré sections for a binary with $\mu = 0.3$, $C = 3$ are shown in panels: (a) at a large scale, (b) at an intermediate scale, (c) close-up in the vicinity of the primary mass. Panel (d) shows the Poincaré section for $\mu = 0.5$ and $C = 3$. Red regions are forbidden since there $\dot{x}^2 + \dot{y}^2 < 0$. Black dots represent non-escaped orbits staying inside the $r < R_s = 10$ region after time $t = 10$. Invariant KAM curves (blue dots) are obtained choosing initial conditions inside KAM islands. The red (blue) star $*$ $(*)$ gives the position of the $1 - \mu$ mass (μ mass). The Poincaré section is obtained with orbits of $N = 10^7$ test particles initially placed at random in the region $1.3 \leq r \leq 2.5$. Particles as escaped once $r > R_S$.

where x and y are the test particle coordinates, $p_x = \dot{x} - y$ and $p_y = \dot{y} + x$ are the corresponding canonically conjugated momenta, and

$$V(x, y) = -\frac{(1-\mu)}{\left((x-\mu)^2 + y^2\right)^{1/2}} - \frac{\mu}{\left((x+(1-\mu))^2 + y^2\right)^{1/2}} \quad (2)$$

is the gravitational potential of the two primaries. Here the distance between primaries is 1, the total mass $m_1 + m_2 = 1$, the gravitational constant $\mathcal{G} = 1$, consequently the rotation period of the binary is 2π. Hamiltonian (1) with potential (2) represents the Jacobi integral of motion (Jacobi, 1836). In the following we define the Jacobi constant as $C = -2H$. This Jacobi Hamiltonian describes also the planar dynamics of an electrically charged test particle experiencing a perpendicular magnetic field and a classical hydrogen-like atom with a Coulomb-like potential (2).

We aim to study the dynamics of particles evolving on escaping and non-escaping orbits around the binary. We perform intensive numerical integration of the equations of motion derived from Hamiltonian (1) using an adaptive time step 4th order Runge-Kutta algorithm with Levi-Civita regularization in the vicinity of the primaries (Levi-Civita, 1920). The achieved accuracy is such as the integral of motion relative error is less than 10^{-9} (10^{-5}) for more than 91% (99%) of integration steps. For different Jacobi constants C, we randomly inject up to 10^8 test particles in the $1.3 \leq r \leq 2.5$ ring with initial radial velocity $\dot{r} = 0$ and initial angular velocity $\dot{\phi} < 0$ (r and ϕ are polar coordinates in the synodic frame). Each test particle trajectory is followed until the integration time attains $t_S = 10^4$ or until the region $r > R_S = 10$ is reached where we consider that test particles are escaped (ionized) from the binary.

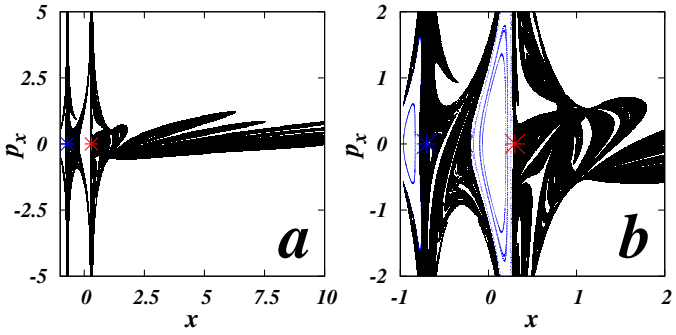

Figure 2: (p_x, x) - Poincaré section of the Jacobi Hamiltonian (1) with $y = 0$ and $p_y > 0$ for a binary with $\mu = 0.3$, $C = 3$ (corresponding to Fig. 1a, b, c). Panel (a): Poincaré section at large scale; panel (b): zoom in the vicinity of primaries. Black dots represent non-escaped orbits staying inside the $r < R_s = 10$ region after time $t = 10$. Blue dots represent bounded orbits inside stability islands. The red (blue) star $*$ $(*)$ gives the position of the primary (secondary) mass as in Fig. 1. The Poincaré section is obtained with the same orbits as in Fig. 1.

3. Strange repeller structures

In phase space, orbits are embedded in a three-dimensional surface defined by the Jacobi constant C. In order to monitor particle trajectories we choose a two-dimensional surface defined by an additional condition. Here we choose either the condition $(\dot{r} = 0, \dot{\phi} < 0)$ to represent Poincaré section as a (x, y)-plane (Figs. 1,5,6,7 and 10) or the condition $(y = 0, p_y > 0)$ to represent Poincaré section as a (p_x, x)-plane (Fig. 2). A similar approach was also used in Nagler (2004, 2005).

We show in Fig. 1 (panels a, b, c) an example of (x, y) - Poincaré section of the Jacobi Hamiltonian (1) for mass parameter $\mu = 0.3$ and Jacobi constant $C = 3$. Red regions correspond to forbidden zones where particles would have imaginary velocities. Inside central islands in the close vicinity of primaries blue points mark out regular and chaotic orbits of bounded motion. In particular, the KAM invariant curves (Lichtenberg and Lieberman, 1992) can be seen *e.g.* in Fig. 1c. In Fig. 1a, the trace of non-escaped chaotic orbits (black points) remaining inside the disk $r < R_S = 10$ after time $t = 10$ defines a set of points forming two spiral arms centered on the binary center of mass. This set has a spiral structure of strange repeller since orbits in its close vicinity rapidly move away from the set and consequently from the binary. The fractal property results in a self-similar structure clearly seen by zooming to smaller and smaller scales (see Fig. 1a, b, c). This fractal structure remains stable in respect to moderate variation of mass ratio μ as it is illustrated in Fig. 1 (panels b, d). A strange repeller structure is also clearly visible in the corresponding Poincaré section in (p_x, x) plane shown in Fig. 2 for $\mu = 0.3$, $C = 3$.

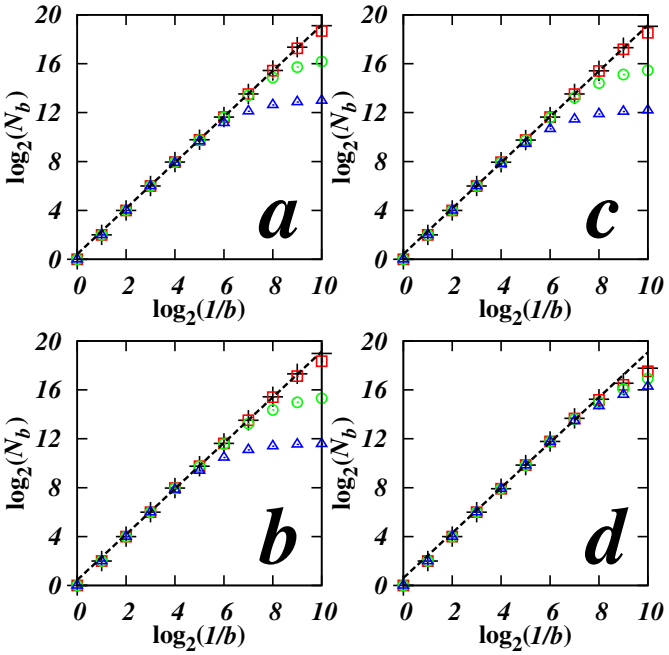

Figure 3: Number of boxes N_b covering at scale b non-escaped orbits structure (strange repeller) appearing in (x, y) - Poincaré section of the Jacobi Hamiltonian (1). Box-counting computation is performed in an annulus square consisting in a square region $-3.9 \leq x, y \leq 3.9$ deprived of its central square region $-1.3 \leq x, y \leq 1.3$. The annulus square is divided into 8 equal square areas of linear size $dl_0 = 1.3$. We average the box counting N_b over the 8 squares. At scale b each square is divided into $1/b^2$ boxes of linear size $dl = b\, dl_0$. Box-counting results are shown for Poincaré section of orbits staying in the $r < R_S = 10$ disk after $t = 3$ (black crosses), $t = 10$ (red squares), $t = 30$ (green circles), $t = 50$ (blue triangles). The fractal dimension D of the strange repeller is the slope of the affine function $\log_2 N_b = f(\log_2(1/b))$. Keeping orbits staying in the $r < R_S$ disk after time $t = 10$ ($t = 3$) we obtain a strange repeller fractal dimension (a) $D = 1.8711 \pm 0.0100$ ($D = 1.8732 \pm 0.0105$) for $\mu = 0.3$ and $C = 3$ (see Fig. $1a, b, c$), (b) $D = 1.8657 \pm 0.0117$ ($D = 1.8690 \pm 0.0129$) for $\mu = 0.4$ and $C = 3$ (see Fig. $10b$), (c) $D = 1.8700 \pm 0.0077$ ($D = 1.8722 \pm 0.0084$) for $\mu = 0.3$ and $C = 2.6$ (see Fig. $5a$), (d) $D = 1.8349 \pm 0.0484$ ($D = 1.8464 \pm 0.0436$) for $\mu = 0.3$ and $C = 3.4$ (see Fig. $5d$). Fits have been performed in the scale range $2^4 \leq 1/b \leq 2^8$. We used $N = 10^8$ (a, b, c), $N = 10^6$ (d) test particles initially distributed at random in the $1.3 \leq r \leq 2.5$ ring. The fractal dimension has been computed with (a) $N_{t>3} = 39526570$, $N_{t>10} = 9933333$, $N_{t>30} = 768282$, $N_{t>50} = 83290$ points, (b) $N_{t>3} = 26743797$, $N_{t>10} = 6550163$, $N_{t>30} = 372871$, $N_{t>50} = 25037$ points, (c) $N_{t>3} = 37610948$, $N_{t>10} = 8721338$, $N_{t>30} = 419296$, $N_{t>50} = 39891$ points, (d) $N_{t>3} = 8569720$, $N_{t>10} = 5447406$, $N_{t>30} = 2245927$, $N_{t>50} = 1083887$ points. The curves bend down for the smallest scales b when $1/b^2$ becomes of the order of the number of collected points in Poincaré section.

The fractal dimension of the strange repeller is determined using box-counting method (Lichtenberg and Lieberman, 1992; Ott, 1993) as $D = \lim_{b \to 0} \ln N_b / \ln(1/b)$ where N_b is at scale b the number of at least once visited boxes in the Poincaré section. The box-counting fractal dimension of the strange repeller presented in Fig. $1a, b, c$ is $D \approx 1.87$ (Fig. $3a$). This fractal dimension value is computed from the strange repeller structure formed by orbits staying in the disk $r < R_S = 10$ after time $t = 10$. We see from Fig. 3 that the fractal dimension remains practically the same for the parameters considered here $\mu = 0.3, 0.4$ and $C = 2.6, 3, 3.4$. When the escape radius is increased up to $R_S = 100$ (Fig. 4) the fractal dimension value is the same as for an escape radius $R_S = 10$ (Fig. 3). Thus

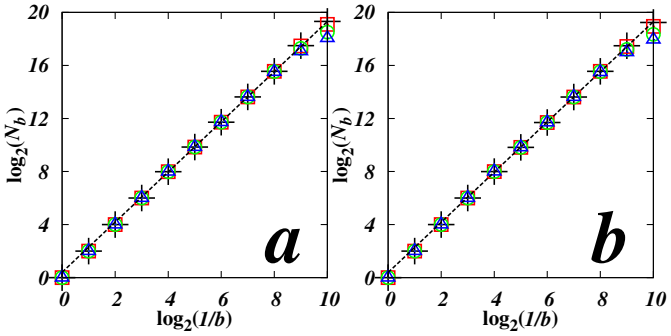

Figure 4: Number of boxes N_b covering at scale b non-escaped orbits structure (strange repeller) appearing in (x, y) - Poincaré section of the Jacobi Hamiltonian (1). Box-counting computation is performed as in Fig. 3. Box-counting results are shown for Poincaré section of orbits staying in the $r < R_S = 100$ disk after $t = 3$ (black crosses), $t = 10$ (red squares), $t = 30$ (green circles), $t = 50$ (blue triangles). Keeping orbits staying in the $r < R_S = 100$ disk after time $t = 3, 10, 30, 50$ we obtain a strange repeller fractal dimension (a) $D = 1.8908 \pm 0.00876, 1.8900 \pm 0.00858, 1.8874 \pm 0.00754, 1.8799 \pm 0.00480$ for $\mu = 0.3$ and $C = 3$ (see Fig. $1a, b, c$), (b) $D = 1.8916 \pm 0.0129, 1.8911 \pm 0.0127, 1.8869 \pm 0.0110, 1.8786 \pm 0.0086$ for $\mu = 0.4$ and $C = 3$ (see Fig. $10b$). Fits have been performed in the scale range $2^4 \leq 1/b \leq 2^8$. We used $N = 10^8$ test particles initially distributed at random in the $1.3 \leq r \leq 2.5$ ring. The fractal dimension has been computed with (a) $N_{t>3} = 38090345$, $N_{t>10} = 18470667$, $N_{t>30} = 7588914$, $N_{t>50} = 4574705$ points, (b) $N_{t>3} = 27206778$, $N_{t>10} = 14259496$, $N_{t>30} = 6542192$, $N_{t>50} = 4286763$ points.

the obtained value of D is not affected by the escape cut-off distance R_S. Also, as seen in Fig. 4, the fractal dimension remains practically the same if we consider strange repeller structures obtained after time $t = 3$, 10, 30 and 50. Hence even for short times the strange repeller structure is already well defined and perdures for greater times since D is constant (at least here up to $t = 50$). Throughout this work, for the sake of clarity we choose to present Poincaré sections for orbits staying in the $r < R_S = 10$ disk after time $t = 10$.

Fig. 5 shows (x, y) - Poincaré sections for the mass parameter $\mu = 0.3$ and for different Jacobi constants from $C = 2.6$ to $C = 4$. The strange repeller structure constituted by non-escaping orbits is progressively expelled from the primaries vicinity as C increases. At $C = 2.6$, 3, 3.2, 3.4 (Fig. $5a, b, c, d$) non-escaping trajectories may still pass close by each one of the primaries. The strange repeller still dominates the phase portrait with a fractal dimension decreasing down to $D \approx 1.84$ for $C = 3.4$ (Fig. $3d$). For greater values $C = 3.6$, 4 (Fig. $5e, f$) the forbidden zone insulates the immediate vicinity of the primaries from trajectories coming from regions beyond $r \sim 1$. Regular and chaotic trajectories corresponding to particles gravitating one or the two primaries are confined in the very central region (Valtonen and Karttunen, 2006). The strange repeller is confined in a narrow ring located in the region $r \sim 1.5$. Beyond that region we observe nearly stable circular orbits (blue dots) corresponding to particles gravitating the whole binary with a radius $r \sim 2$. For these orbits stable means that these orbits have not escaped from the disk $r < R_S$ during the whole integration duration t_S.

Unless otherwise stated, we have deliberately omitted the class of orbits crashing primaries. According to Nagler (2004, 2005) the crash basin scales as a power law r_b^α where r_b is the

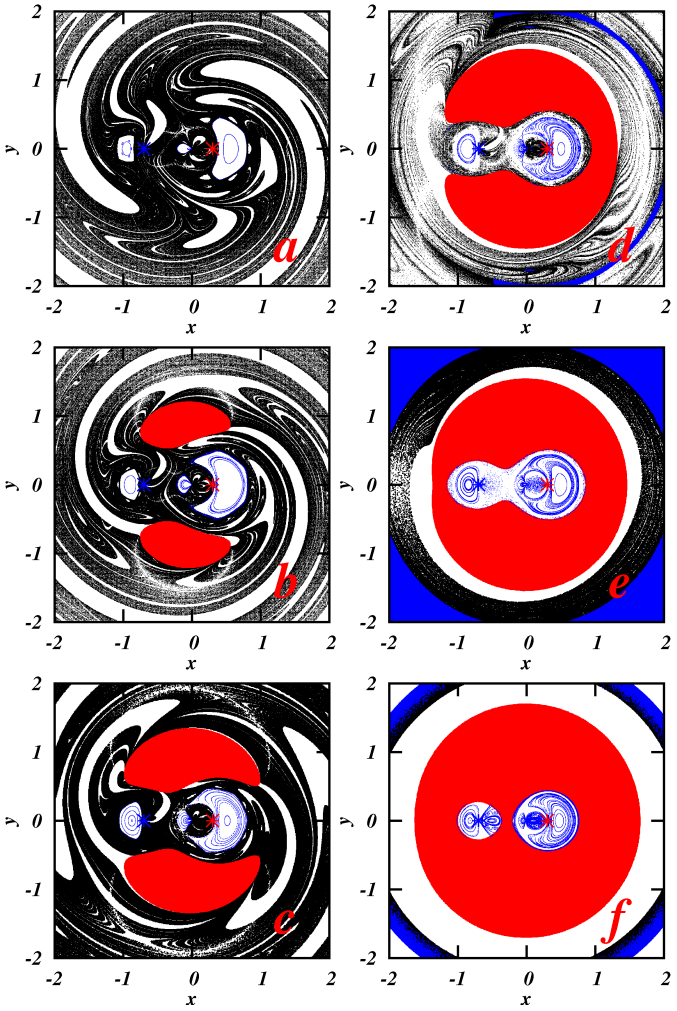

Figure 5: (x, y) - Poincaré sections of the Jacobi Hamiltonian (1) with $\dot{r} = 0$ and $\dot{\phi} < 0$ for $\mu = 0.3$ and Jacobi constant (a) $C = 2.6$, (b) $C = 3$, (c) $C = 3.2$, (d) $C = 3.4$, (e) $C = 3.6$, and (f) $C = 4$. Red regions are forbidden since there $\dot{x}^2 + \dot{y}^2 < 0$. Black dots represent non-escaped orbits staying inside the $r < R_s = 10$ region after time $t = 10$. Blue dots represent bounded orbits. The red (blue) star $*$ ($*$) gives the position of the primary (secondary) mass as in Fig. 1. Poincaré sections have been obtained analyzing orbits of $N = 10^7$ (a, b, c) and $N = 10^5$ (d, e, f) particles initially placed in the $1.3 \leq r \leq 2.5$ region. Particles are considered as escaped once $r > R_S$.

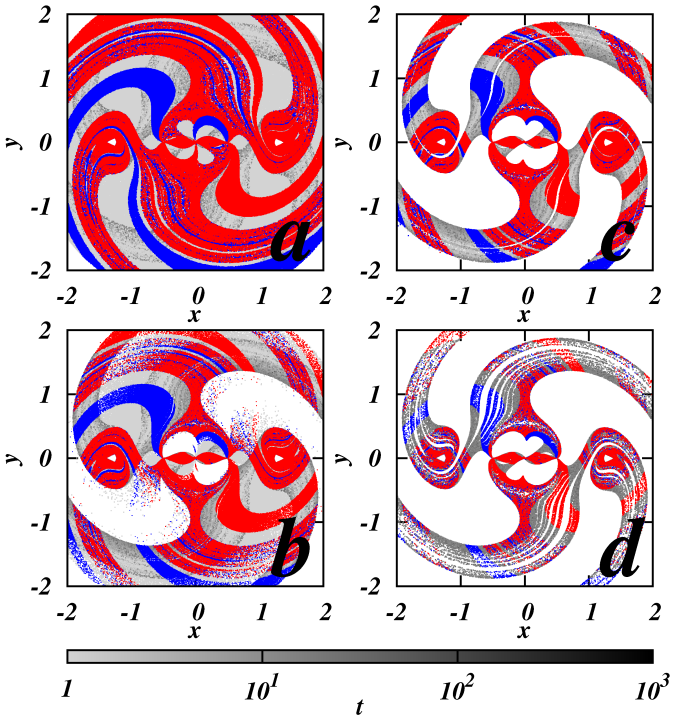

Figure 6: (x, y) - Poincaré sections of the Jacobi Hamiltonian (1) with $\dot{r} = 0$ and $\dot{\phi} < 0$ for primary bodies with radius $r_b = 0.01$ and for $\mu = 0.5$ and $C = 1$. The panels show traces of orbits associated with particles escaping at time (a) $t_{esc} > 0$ (*i.e.* all computed orbits are shown), (b) $t_{esc} > 0.01$, (c) $t_{esc} > 1$, (d) $t_{esc} > 10$. The gray scale bar shows the time when particles pass through the Poincaré section. Light gray (dark gray) points have been obtained at $t \approx 1$ ($t \approx 10^3$). Red (blue) points have been obtained from orbits crashing on the μ (1-μ) primary mass. Initially 10^6 particles have been randomly distributed in the $1.3 \leq r \leq 2.5$ ring. Fig. 5 (4th panel for $r_b = 0.01$) in Nagler (2004) is similar to panel (a).

radius of the primary mass and $\alpha \sim 0.5$. In this work we choose a radius of $r_b = 10^{-5}$ for the two primaries which gives two percent of crashing orbits and an area of about one percent for crash basin not visible in the presented Poincaré sections. The sets of non-escaping orbits shown in Fig. 1 are also distinguishable in the studies (Nagler, 2004, 2005) devoted to crashing orbits but not studied in details. For example Fig. 1d presents a Poincaré section for the Copenhagen problem case ($\mu = 0.5$) with $C = 3$ which is similar to the Poincaré section presented in the study (Nagler, 2004) Fig. 3 right column middle row for $C = 2.85$.

The time evolution of density of non-escaped particles is shown in Fig. 6 for $\mu = 0.5$ and Fig. 7 for $\mu = 0.3$ for the case of primary bodies of relatively large radius $r_b = 0.01$ (such a size is also available in Fig. 5 in Nagler (2004)). These data clearly show that the strange repeller structure is established on rather short time scales with $t \sim 1$. We also see that for such a value of r_b the measure of crashed orbits gives a visible contribution to the measure of non-escaping orbits of strange repeller.

Finally we note that in our computations we determined the fractal dimension D of trajectories non-escaping in future (see a similar situation considered for the Chirikov standard map with absorption in Ermann, L. and Shepelyansky, D. L., 2010). According to the general relations known for the strange fractal sets in dynamical systems the fractal dimension D_0 of the invariant repeller set (orbits non-escaping neither in the future nor in the past) satisfies the relation $D_0 = 2(D - 1)$ (Ott, 1993). Thus for the typical value we have in Fig. 1 at $\mu = 0.3$ with $D \approx 1.87$ we obtain $D_0 \approx 1.74$.

We can expect that the spiral fractal structure, clearly present in the plane (x, y) of the Poincaré sections (see e.g. Fig. 1), will give somewhat similar traces for the surface (or area) density $\rho_s = dN_t/dxdy$ of particles N_t remaining in the system at an instant moment of time t. A typical example of surface density, corresponding to Fig. 1a, b, c, is shown in Fig. 8. Indeed, we find a clear spiral structure of $\rho_s(x, y)$ similar to the spiral structure of the strange repeller of Fig. 1a, b, c. Of course, here in Fig. 8 we have the projected density of particles in (x, y) plane taken at all values of $\dot{r}$ (and not only at $\dot{r} = 0$ as in Fig. 1), This

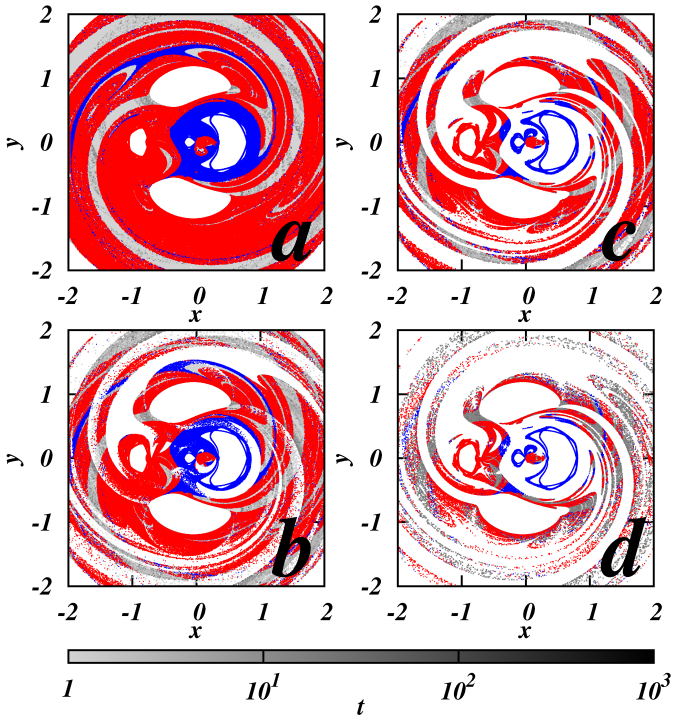

Figure 7: (x, y) - Poincaré sections of the Jacobi Hamiltonian (1) with $\dot{r} = 0$ and $\dot{\phi} < 0$ for primary bodies with radius $r_b = 0.01$ and for $\mu = 0.3$ and $C = 3$. The panels show (a) all points after $t = 0$, (b) all points after $t = 0.01$, (c) all points after $t = 1$, (d) all points after $t = 10$. The gray scale bar shows the time when particles pass through the Poincaré section. Light gray (dark gray) points have been obtained at $t \approx 1$ ($t \approx 10^3$). Red (blue) points have been obtained from orbits crashing on the μ (1-μ) primary mass. Initially 10^5 particles have been randomly distributed in the $1.3 \le r \le 2.5$ ring.

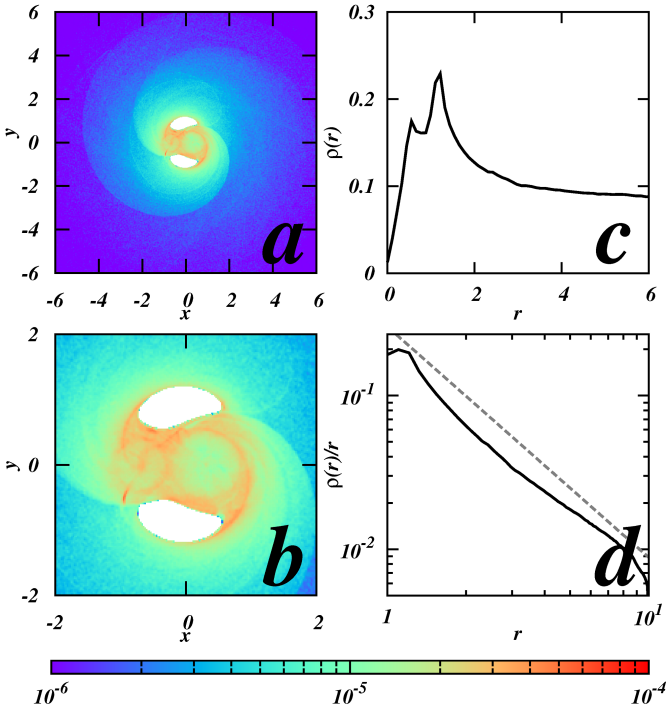

Figure 8: (a) Snapshot of the remaining particles at $t = 10$ for $\mu = 0.3$ and $C = 3$. The number of particles initially injected in the $1.3 \le r \le 2.5$ ring is $N = 10^8$, at time $t = 10$ there are $N_t = 13302225$ particles remaining inside the circle $r \le R_S = 10$, colors show the surface density of particles ρ_s in the plane (x, y), color bar gives the logarithmic color scale of density with levels corresponding to a proportion of the N_t remaining particles; (b) same as panel (a) but on a smaller scale; (c) linear density $\rho(r) = dN_t/dr$; (d) angle averaged surface density $\rho(r)/r = 2\pi < \rho_s(r) >$, the dashed line shows the slope $\propto 1/r^{3/2}$.

leads to a smoothing of the fractal structure of the Poincaré section but the spiral distribution of density ρ_s remains well visible. We also note that the angle averaged density of remaining particles $< \rho_s(r) > \propto 1/r^{3/2}$ has a radial dependence on r being similar to those found for the dark matter density obtained in the symplectic simulations of scattering and capture of dark matter particles on binary system (see e.g. Fig. 4a in Lages and Shepelyansky, 2013; Rollin et al., 2015b).

4. Poincaré recurrences and probability decay

We determine numerically the probability $P(t)$ to stay inside the system for time larger than t. For that N particles are randomly distributed in the range $1.3 \le r \le 2.5$ and then the survival probability $P(t)$ is defined as the ratio $P(t) = N_t/N$, where N_t is the number of particles remained inside the system with $r < R_S = 10$ at times larger than t. This survival probability is proportional to the integrated probability of Poincaré recurrences (see e.g. Chirikov and Shepelyansky, 1999; Frahm, K. M. and Shepelyansky, D. L., 2010).

The typical examples of the decay $P(t)$ are shown in Fig. 9. At relatively small time scales with $t < 100$ the decay can be approximately described by an exponential decay with a decay time $\tau_s \sim 10$. Indeed, for the strange dynamical sets (e.g. strange attractors) one obtains usually an exponential decay since there are no specific sticking regions in such strange sets (Chirikov and Shepelyansky, 1984).

However, at larger time scales $t > 100$ we see the appearance of the algebraic decay of probability corresponding to the algebraic statistics of Poincaré recurrences discussed for symplectic maps (see e.g. Chirikov and Shepelyansky, 1999; Cristadoro and Ketzmerick, 2008; Frahm, K. M. and Shepelyansky, D. L., 2010). When the decay time is measured in number of crossings of the Poincaré section n we obtain the Poincaré exponent β of this decay $\beta = 1.49$ being close to the values $\beta \approx 1.5$ found in the symplectic maps. However, if the time is measured in number of rotations of binaries $t/2\pi$ then we find a somewhat large value of β (see Fig. 9). We explain this deviation a bit later.

The properties of orbits surviving in the system for long times are shown in Fig. 10. We see that such orbits are concentrated in the vicinity of critical KAM curves which separate the orbits of strange repeller from the integrable islands with KAM curves. This is exactly the situation discussed in the symplectic maps (see e.g. Chirikov and Shepelyansky, 1999; Cristadoro and Ketzmerick, 2008; Frahm, K. M. and Shepelyansky, D. L., 2010). Thus the asymptotic decay of survival probability is determined by long time sticking orbits in the vicinity of critical KAM curves. The detail analytical explanation of this generic phenomenon is still under debates (see e.g. Meiss, 2015).

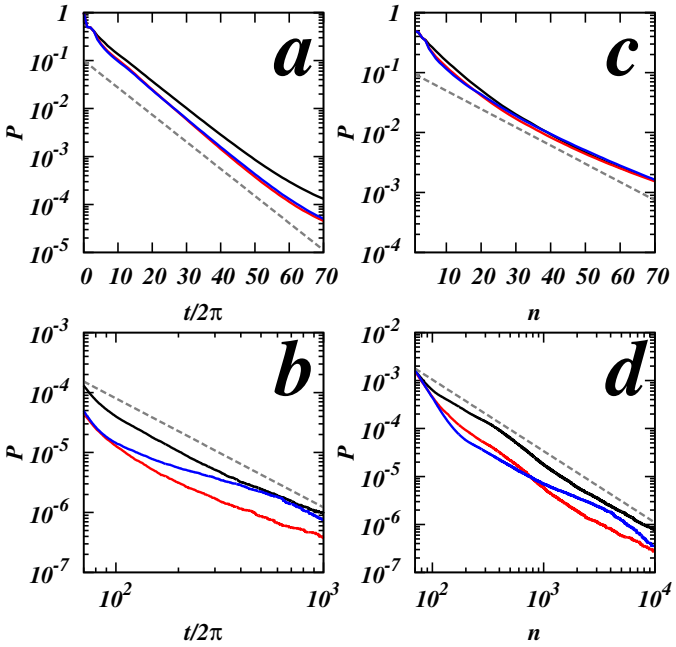

Figure 9: Survival probability P of particles as a function of time t (left panels, binary period is 2π) and as a function of the number n of successive Poincaré section crossings (right panels) for $C = 3$ and binaries with mass parameter $\mu = 0.3$ (black curve), $\mu = 0.4$ (red curve), $\mu = 0.5$ (blue curve). Survival probabilities are shown in semi-log scale (top panels) and in log-log scale (bottom panels). Dashed lines show (a) exponential decay $P \propto \exp(-t/\tau_s)$ with $1/\tau_s = 0.13$, (b) algebraic decay $P(t) \propto 1/t^{\beta}$ with the Poincaré exponent $\beta = 1.82$, (c) exponential decay $P(n) \propto \exp(-n/\tau_s)$ with $1/\tau_s = 0.07$, (d) algebraic decay $P(n) \propto 1/n^{\beta}$ with $\beta = 1.49$. Initially 10^8 particles have been randomly distributed in the $1.3 \leq r \leq 2.5$ ring. Escape radius is $R_S = 10$.

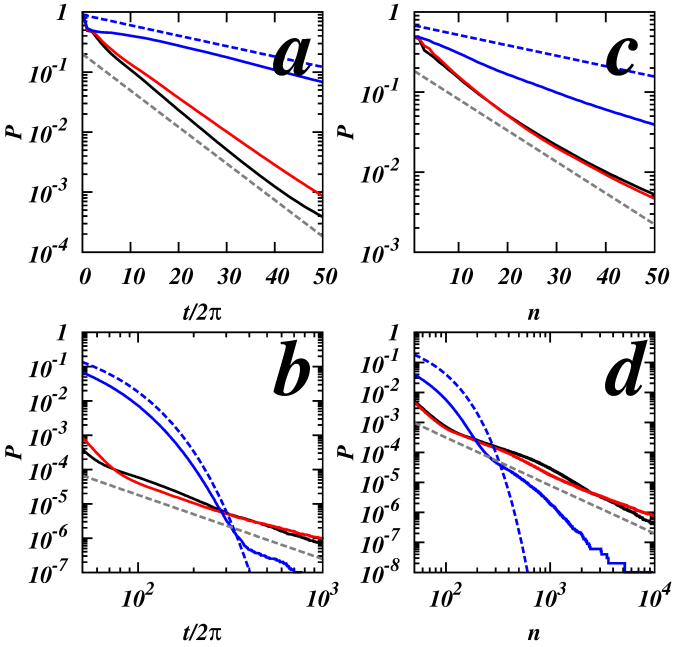

Figure 11: Survival probability P of particles as a function of time t (left panels, binary period is 2π) and as a function of the number n of successive Poincaré section crossings (right panels) for $\mu = 0.3$ and $C = 2.6$ (black curve), $C = 3$ (red curve), $C = 3.4$ (blue curve). Survival probabilities are shown in lin-log scale (top panels) and in log-log scale (bottom panels). Blue dashed lines show exponential decay $P(t) \propto \exp(-t/\tau_s)$ with $1/\tau_s = 0.04$ (a,b) and $P(n) \propto \exp(-n/\tau_s)$ with $1/\tau_s = 0.03$ (c,d). Gray dashed lines show (a) exponential decay $P(t)$ with $1/\tau_s = 0.14$, (b) algebraic decay $P(t)$ with $\beta = 1.87$, (c) exponential decay $P(n)$ with $1/\tau_s = 0.09$, (d) algebraic decay $P(n)$ with $\beta = 1.6$. Initially 10^8 particles have been randomly distributed in the $1.3 \leq r \leq 2.5$ ring. Escape radius is $R_S = 10$.

At fixed $\mu = 0.3$ the variation of decay properties of $P(t)$ with the Jacobi constant C is shown in Fig. 11. For $C = 3.4$ the exponential decay of $P(t)$ is much slower than for the cases $C = 3.6$ and $C = 3$ (there is a factor 3.5 between corresponding characteristic time scales τ_s). We attribute this behavior to the

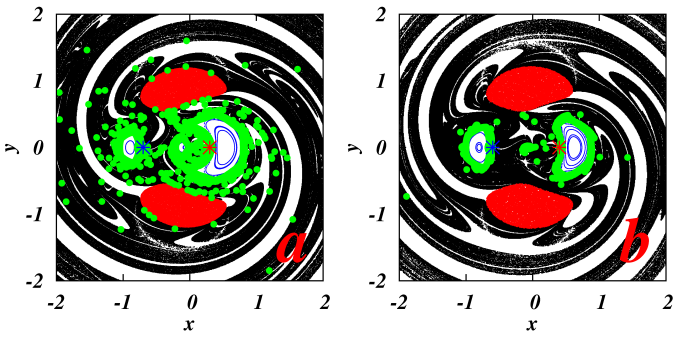

Figure 10: (x, y) - Poincaré sections of the Jacobi Hamiltonian (1) with $\dot{r} = 0$ and $\dot{\phi} < 0$ for $C = 3$ in the case of (a) a $\mu = 0.3$ binary and (b) a $\mu = 0.4$ binary. Red regions are forbidden since there $\dot{x}^2 + \dot{y}^2 < 0$. Black dots represent non-escaped orbits staying inside the $r < R_S = 10$ region after time $t = 10$. Blue dots represent bounded orbits on KAM curves inside integrable islands. Green plain circles mark out non-escaped orbits remaining inside the disk $r < R_s$ after time $t = 500$. The red (blue) star $*$ ($*$) gives the position of the primary (secondary) mass. Each of Poincaré sections is obtained from orbits of $N = 10^7$ particles initially placed in the $1.3 \leq r \leq 2.5$ region; these particles are considered as escaped once $r > R_s$.

fact that the forbidden zone encloses almost completely binary components letting for particles only a small route to binary components in comparison with cases $C = 2.6$ and $C = 3$ for which the route to gravitational perturbers is not constrained. Meanwhile, particles have a limited access to the chaotic component (see Fig. 5d where it forms a narrow peanut shell around central stability islands) so that the sticking in the vicinity of critical KAM curves is reduced emphasizing the exponential decay. For $C = 2.6, 3$ at long time scales (Fig. 11d) we have a well visible algebraic decay $P(n)$ with $\beta \sim 1.5$ (we may assume that increasing sufficiently the number of initially injected particle for the case $C = 3.4$, blue line in Fig. 11d would also exhibit at large time scales the same $\beta \sim 1.5$ algebraic decay). However, algebraic decay of $P(t)$ for $C = 2.6, 3$ at large time scale (Fig. 11b) still have somewhat different value of β.

The origin of this difference for $P(t)$ becomes clear from Fig. 12 where we show the data similar to those of Figs. 9,11 at $\mu = 0.3$ but with the escape radius $R_S = 100$. We see that the decay properties of $P(n)$ remain practically unchanged that confirms the generic features of obtained results for β (indeed, stability islands do not affect dynamics at $r \sim R_S = 100$). However, the value of β for $P(t)$ is significantly reduced to $\beta \approx 1.1$. We explain this by the fact that in the usual time units the measure of chaotic component at large distances becomes dominant and the escape time is determined simply by a Kepler rotation

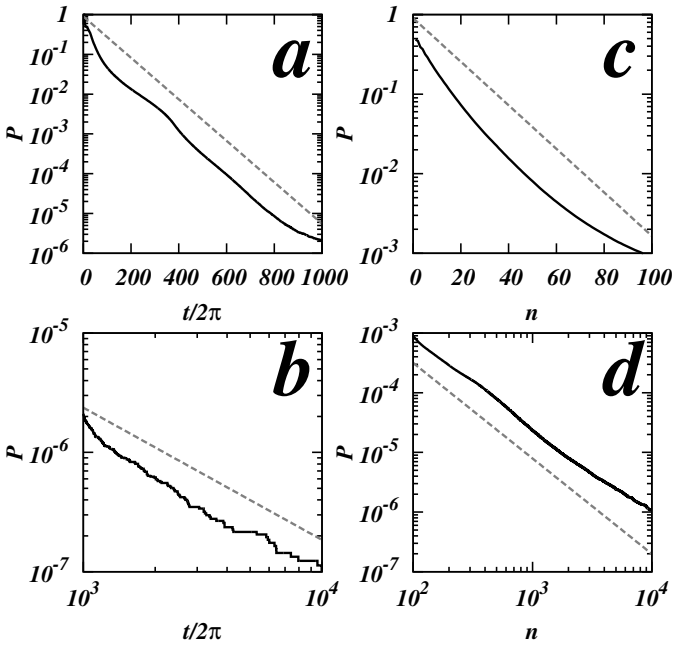

Figure 12: Survival probability P of particles as a function of time t (left panels, binary period is 2π) and as a function of the number n of successive Poincaré section crossings (right panels) for $\mu = 0.3$, $C = 3$ in the case of an escape radius $R_S = 100$. Dashed curves show (a) exponential decay $P(t)$ with $1/\tau_s = 0.012$, (b) algebraic decay $P(t)$ with $\beta = 1.11$, (c) exponential decay $P(n)$ with $1/\tau_s = 0.062$, (d) algebraic decay $P(n)$ with $\beta = 1.40$. Initially 10^8 particles have been randomly distributed in the $1.3 \le r \le 2.5$ ring.

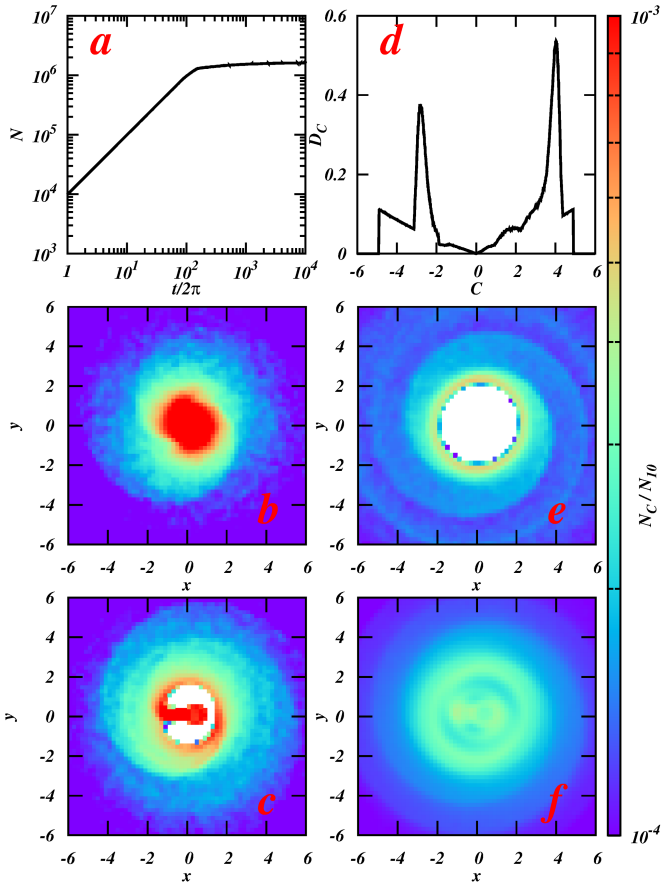

Figure 13: Density of particles in the steady state. (a) Number N of particles in the $r < 100$ region of the binary as a function of time t. We have continuously injected $N = 10^8$ particles placed randomly on $r = 100$ circle with close to parabolic but hyperbolic trajectories in the 2-body paradigm. Steady state is achieved around $t \sim t_0 = 10^3$. The surface density of particles $\rho_s(x, y)$ is shown for Jacobi constants $C = 2.6$ (b), $C = 3.4$ (c) and $C = 4$ (e). Each surface density has been obtained from 1000 surface density snapshots taken at regular time interval after $t_0 = 10^3$ once steady state is attained. Color bar gives the logarithmic color scale of density with levels corresponding to the ratio of N_C/N_{10} where N_C is the number of particles in a given cell of size 0.1×0.1 and N_{10} is the number of particles in the $r < 10$ region. Panel (d) shows the normalized steady state distribution of Jacobi constants of particles present in the $r < 100$ region. Panel (f) shows the steady state surface density build with all particles in $r < 100$ region.

period which becomes larger for large r values. This leads to the decay exponent $\beta = 2/3$ for $P(t)$ as discussed in Borgonovi et al. (1988) and explains the variation of β with R_S. However, when the time is counted in the number of orbital periods the divergence of the orbital period at large r values (or small coupling energies) does not affect the decay and we obtain the Poincaré exponent $\beta \approx 1.5$ being independent of R_S.

We note that the recent studies of survival probability decay in the PCRTBP also report the value of $\beta \approx 1.5$ (Kovács and Regály, 2015).

5. Symplectic map description

Finally we discuss the case when particles in the sidereal reference frame scatter on the binary with relatively large values of perihelion distance $q \gg 1$. Such a case corresponds to large $|C| \gg 1$. For $q \gg 1$ the dynamics of particle in the field of two binaries is approximately described by the symplectic map of the form $\bar{w} = w + F(x); \bar{x} = x + \bar{w}^{-3/2}$ where $w = -2E$ is the particle energy, x is the phase of binary rotation (in units of 2π) when the particle is located at its perihelion and $F(x) \propto \mu$ is a periodic function of x (Petrosky, 1986; Chirikov and Vecheslavov, 1989; Shevchenko, 2011; Rollin et al., 2015a,b); bars above w and x mark new values after one rotation around the binary. The amplitude F_{max} decreases exponentially with increasing q. Usually, one considers the case of $\mu \ll 1$ (e.g. Sun and Jupiter) but our studies show that this form remains valid even for $\mu \sim 0.5$ if $q \gg 1$. At $\mu \ll 1$ we have $F_{max} \ll 1$ and the escape time t_i becomes very large $t_i \propto 1/{F_{max}}^2$ being much larger than the Lyapunov time scale. In this situation the fractal dimensions D and D_0 are very close to $D = D_0 = 2$ (Ott, 1993; Ermann, L. and Shepelyansky, D. L., 2010) and the fractal effects practically disappear. Due to that this case is not interesting for the fractal analysis.

6. Discussion

We analyzed the PCRTBP dynamical system and showed that for moderate mass ratio of primary bodies $\mu \sim 0.5$ the Poincaré section is characterized by a strange repeller with the fractal dimension having typical values $D \approx 1.87$ ($D_0 \approx 1.74$) at moderate values of the Jacobi constant $C \sim 2$. At the same time certain islands of integrable motion are still present. Such a struc-

ture of the Poincaré section leads to an exponential decay of survival probability in the system on short time scales followed by the algebraic decay with the Poincaré exponent $\beta \approx 1.5$ being similar to the values known for the statistics of Poincaré recurrences in generic symplectic maps. For the small mass ratio $\mu \ll 1$ the escape times becomes very large and the fractal dimension becomes close to the usual value $D = 2$.

It is interesting to note that the strange repeller structure (see Figs. 1,5,6,7,10) reminds the structure of spiral galaxies (see e.g. Milky Way representation at European Southern Observatory website, 2013). In fact the fractal features of galaxies have been studied extensively by various groups (Elmegreen and Elmegreen, 2001; Sánchez et al., 2007, 2010) which obtained from observation data the fractal dimensions for the plane density being around $D_g \approx 1.3 - 1.7$ for different galaxies. Some of these values (e.g. Sánchez et al., 2007, with $D_g \approx 1.7$) are similar to those obtained here for the Poincaré section of PCRTBP. Our results show that the spiral fractal structure of the Poincaré section of PCRTBP leads to a spiral structure of global density of particles ρ_s remaining in the system (see Fig. 8). Thus we make a conjecture that the spiral structure of certain galaxies can be linked to the underlying spiral fractals appearing in the dynamics of particles in binary systems. Of course, such a conjecture requires more detailed analysis beyond the present paper such as taking into account the third dimension. Also whether or not the spiral structure remains in the steady state is an important question. To bring some elements of response to the latter question we have injected at $r = 100$ particles with close-to-parabolic hyperbolic trajectories in 2-body paradigm. We use a Maxwellian distribution for initial velocities $f(v)dv = \sqrt{54/\pi}\left(v^2/u^3\right)\exp\left(-3v^2/2u^2\right)dv$ with $u = 0.035$ and a homogeneous distribution for perihelion $q \in [0; 3]$ parameters. We checked that our results in steady state are independent of initial distributions. We present on Fig. 13 the surface density of particles $\rho_s(x, y)$ in the steady state attained around $t_0 \sim 10^3$ (Fig. 13a). We clearly see that the two arms spiral structure remains in the steady state, we show examples for particles with trajectories characterized by (b) $C = 2.6$, (c) $C = 3.4$, (e) $C = 4$ (example not shown for $C = 3$ is analogous to Fig 8a). However when all injected particles are considered independently of the Jacobi constant C we obtain a blurred spiral (Fig. 13f). The contributions of different Jacobi constants are consequently mixed according to the distribution Fig. 13d. We remark that the results presented in Fig. 13 share similarities with those obtained in the study of chaotic trajectories in spiral galaxies (Harsoula et al., 2011; Contopoulos and Harsoula, 2012, 2013). On the basis of obtained results we make a conjecture about existence of certain links between observed fractal dimensions of galaxies (Elmegreen and Elmegreen, 2001; Sánchez et al., 2007, 2010) and fractal spiral repeller structure studied here. We think that the further studies of fractal structures in binary systems will bring new interesting results.

Altmann, E. G., Portela, J. S. E., Tél, T., May 2013. Leaking chaotic systems. Rev. Mod. Phys. 85, 869–918.

Astakhov, S. A., Farrelly, D., 2004. Capture and escape in the elliptic restricted three-body problem. Monthly Notices of the Royal Astronomical Society 354 (4), 971–979.

Astakhov, S. A., Lee, E. A., Farrelly, D., 2005. Formation of kuiper-belt binaries through multiple chaotic scattering encounters with low-mass intruders. Monthly Notices of the Royal Astronomical Society 360 (2), 401–415.

Barrio, R., Blesa, F., Serrano, S., 2009. Periodic, escape and chaotic orbits in the Copenhagen and the (n + 1)-body ring problems. Communications in Nonlinear Science and Numerical Simulation 14 (5), 2229 – 2238.

Borgonovi, F., Guarneri, I., Sempio, P., 1988. Long-time decay properties of Kepler map. Il Nuovo Cimento B 102, 151.

Chirikov, B., Shepelyansky, D., 1984. Correlation properties of dynamical chaos in Hamiltonian systems. Physica D: Nonlinear Phenomena 13 (3), 395 – 400.

Chirikov, B. V., May 1979. A universal instability of many-dimensional oscillator systems. Physics Report 52, 263–379.

Chirikov, B. V., Shepelyansky, D. L., 1981. Statistics of Poincare recurrences and the structure of the stochastic layer of a nonlinear resonance. Preprint 81-69 Inst. Nuclear Physics, Novosibirk, 1981 [English translation, Princeton Univ. Report No. PPPL-TRANS-133, (1983)].

Chirikov, B. V., Shepelyansky, D. L., Jan 1999. Asymptotic statistics of Poincaré recurrences in Hamiltonian systems with divided phase space. Phys. Rev. Lett. 82, 528–531, ibid. 89, 239402 (2002).

Chirikov, R. V., Vecheslavov, V. V., Aug. 1989. Chaotic dynamics of Comet Halley. A&A 221, 146–154.

Contopoulos, G., Efstathiou, K., 2004. Escapes and recurrence in a simple hamiltonian system. Celestial Mechanics and Dynamical Astronomy 88 (2), 163–183.

Contopoulos, G., Harsoula, M., 2012. Chaotic spiral galaxies. Celestial Mechanics and Dynamical Astronomy 113 (1), 81–94.

Contopoulos, G., Harsoula, M., 2013. 3d chaotic diffusion in barred spiral galaxies. Monthly Notices of the Royal Astronomical Society 436 (2), 1201–1214.

Cristadoro, G., Ketzmerick, R., May 2008. Universality of algebraic decays in Hamiltonian systems. Phys. Rev. Lett. 100, 184101.

de Assis, S., Terra, M., 2014. Escape dynamics and fractal basin boundaries in the planar earthmoon system. Celestial Mechanics and Dynamical Astronomy 120 (2), 105–130.

Elmegreen, B. G., Elmegreen, D. M., 2001. Fractal structure in galactic star fields. The Astronomical Journal 121 (3), 1507.

Ermann, L., Shepelyansky, D. L., 2010. Ulam method and fractal Weyl law for Perron-Frobenius operators. Eur. Phys. J. B 75 (3), 299–304.

Euler, L., 1772. Theoria motuum lunae, nova methodo pertractata una cum tabulis astronomicis. Borussicae directire vicennali et socio acad. Petropoli Paris in. et Lond. Petropoli, typis academiae imperialis scientiarum, [in Latin].

Frahm, K. M., Shepelyansky, D. L., 2010. Ulam method for the Chirikov standard map. Eur. Phys. J. B 76 (1), 57–68.

Harsoula, M., Kalapotharakos, C., Contopoulos, G., 2011. Asymptotic orbits in barred spiral galaxies. Monthly Notices of the Royal Astronomical Society 411 (2), 1111–1126.

Hénon, M., 1997. Generating Families in the Restricted Three-body Problem. No. vol. 1 in Generating Families in the Restricted Three-body Problem. Springer-Verlag.

Hénon, M., 2001. Generating Families in the Restricted Three-Body Problem: II. Quantitative Study of Bifurcations. Generating Families in the Restricted Three-body Problem. Springer.

Jacobi, C., 1836. Sur le mouvement d'un point et sur un cas particulier du problème des trois corps. Comptes Rendus de l'Académie des Sciences de Paris 3, 59–61, [in French].

Karney, C. F., 1983. Long-time correlations in the stochastic regime. Physica D: Nonlinear Phenomena 8 (3), 360 – 380.

Kovács, T., Regály, Z., 2015. Transient chaos and fractal structures in planetary feeding zones. The Astrophysical Journal Letters 798 (1), L9.

Lages, J., Shepelyansky, D. L., 2013. Dark matter chaos in the solar system. Monthly Notices of the Royal Astronomical Society: Letters 430 (1), L25–L29.

Levi-Civita, T., 1920. Sur la régularisation du problme des trois corps. Acta Mathematica 42 (1), 99–144.

Lichtenberg, A., Lieberman, M., 1992. Regular and chaotic dynamics. Applied mathematical sciences. Springer-Verlag.

Makó, Z., Szenkovits, F., Salamon, J., Oláh-Gál, R., 2010. Stable and unstable orbits around Mercury. Celestial Mechanics and Dynamical Astronomy 108 (4), 357–370.

Meiss, J. D., 2015. Thirty years of turnstiles and transport. Chaos 25 (9), –.
Meiss, J. D., Ott, E., Dec 1985. Markov-tree model of intrinsic transport in Hamiltonian systems. Phys. Rev. Lett. 55, 2741–2744.
Milky Way representation at European Southern Observatory website, 2013. `http://cdn.eso.org/images/screen/eso1339e.jpg`.
Nagler, J., Jun 2004. Crash test for the Copenhagen problem. Phys. Rev. E 69, 066218.
Nagler, J., Feb 2005. Crash test for the restricted three-body problem. Phys. Rev. E 71, 026227.
Ott, E., 1993. Chaos in Dynamical Systems. Cambridge University Press.
Petrosky, T., 1986. Chaos and cometary clouds in the solar system. Physics Letters A 117 (7), 328 – 332.
Poincaré, H., 1890. Sur le problème des trois corps et les équations de la dynamique. Acta Mathematica 13, 1, [in French].
Rollin, G., Haag, P., Lages, J., 2015a. Symplectic map description of Halley's comet dynamics. Physics Letters A 379 (1415), 1017 – 1022.
Rollin, G., Lages, J., Shepelyansky, D., 2015b. Chaotic enhancement of dark matter density in binary systems. A&A 576, A40.
Sánchez, N., Alfaro, E. J., Elias, F., Delgado, A. J., Cabrera-Caño, J., 2007. The nature of the Gould belt from a fractal analysis of its stellar population. The Astrophysical Journal 667 (1), 213.
Sánchez, N., nez, N. A., Alfaro, E. J., Odekon, M. C., 2010. The fractal dimension of star-forming regions at different spatial scales in m33. The Astrophysical Journal 720 (1), 541.
Shevchenko, I. I., Jun 2010. Hamiltonian intermittency and Lévy flights in the three-body problem. Phys. Rev. E 81, 066216.
Shevchenko, I. I., 2011. The Kepler map in the three-body problem. New Astronomy 16 (2), 94 – 99.
Szebehely, V., 1967. Theory of orbits. The restricted problem of three bodies. Academic Press, New York and London.
Valtonen, M., Karttunen, H., 2006. The Three-Body Problem. Cambridge University Press.
Zotos, E., 2015. Crash test for the Copenhagen problem with oblateness. Celestial Mechanics and Dynamical Astronomy 122 (1), 75–99.